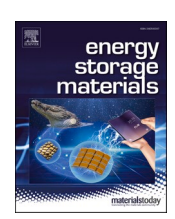
ELSEVIER

Contents lists available at ScienceDirect

# **Energy Storage Materials**

journal homepage: www.elsevier.com/locate/ensm





# A liquid metal interlayer for boosted charge transfer and dendrite-free deposition toward high-performance Zn anodes

Huige Chen <sup>a,1</sup>, Zechu Guo <sup>a,1</sup>, Huashan Wang <sup>a</sup>, Weiyuan Huang <sup>b</sup>, Feng Pan <sup>b,\*</sup>, Ziqi Wang <sup>a,c,\*</sup>

- <sup>a</sup> Department of Materials Science and Engineering, College of Chemistry and Materials Science, Jinan University, Guangzhou 511443, PR China
- <sup>b</sup> School of Advanced Materials, Peking University Shenzhen Graduate School, Shenzhen 518055, PR China
- <sup>c</sup> Guangdong Provincial Key Laboratory of Functional Supramolecular Coordination Materials and Applications, Jinan University, Guangzhou 510632, PR China

# ARTICLE INFO

Keywords: Liquid metal Zn-ion battery Dendrite Zn anode

# ABSTRACT

Metallic Zn is a promising anode for aqueous Zn-ion batteries, but it suffers from dendrite formation, corrosion, and surface passivation during cycling that severely jeopardize the lifetime and charge/discharge kinetics of the battery. Herein, we propose a delayed nucleation strategy to improve the performance of Zn anodes. Through a liquid metal (LM) interlayer, the reduction and deposition of Zn are temporally and spatially separated, and thus fast Zn redox kinetics and dendrite-free Zn (002) deposition can be simultaneously achieved. The accordingly designed flexible anode (Zn@LM-AgT) demonstrates a stabilized Zn plating/stripping cycling over 700 h with a significantly reduced overpotential. When coupled with a vanadium-based cathode, the full cell delivers a sixtimes higher remaining capacity after 1000 cycles than the reference cell. Moreover, flexible batteries with good deformability are also fabricated with the Zn@LM-AgT anode, confirming the practicability of the LM interlayer. The delayed nucleation mechanism provides a novel approach to the high-performance metallic anodes.

# 1. Introduction

Compared with the widely used Li-ion batteries, mild aqueous Zn-ion batteries are cheaper, safer, and more eco-friendly, which have gained significant interests over the past few years. Their anode, metallic Zn, is nontoxic and high-capacity (820 mAh g<sup>-1</sup>), making Zn-ion batteries ideal for wearable devices and grid-scale energy storage [1-4]. However, several drawbacks associated with Zn anodes, such as dendrite growth, corrosion, and surface passivation, severely hinder further advancements in this technology. To be specific, firstly,  $\mathrm{Zn}^{2+}$  ions prefer to deposit on the local inhomogeneities with concentrated charge on the substrate, and eventually form a porous deposition morphology composed of rampant dendrites. With a high elastic modulus (~108 Gpa) [5], Zn dendrites bring the risk of separator penetration and battery short-circuit. In addition, the porous deposition layer produces "dead" Zn easily, which is responsible for the poor cycling life and the deteriorated anode/electrolyte interface. Secondly, Zn is thermodynamically unstable against aqueous electrolytes, meaning that hydrogen evolution reaction (HER) alone with Zn corrosion and passivation is inevitable during battery operation. This not only induces low Coulombic efficiency (CE), but also slows down the interfacial charge

transfer and increases battery resistance.

To tackle the above problems of Zn anodes, various strategies have been employed. For example, functional coating layers such as inorganics [6–8], polymers [9,10], and metal-organic frameworks (MOFs) [11,12] on top of Zn anodes can favor a uniform Zn deposition through modulating Zn<sup>2+</sup> flux or providing zincophilic sites. Three-dimensional (3D) current collectors like Zn sponge [13], Cu foam [14], and porous carbon [15] are able to alleviate dendrite growth by increasing the surface area and reducing the current density of anodes. Deliberately engineered electrolyte compositions with inorganic [16,17] or organic [18,19] additives help reduce the side reactions and stabilize the anode/electrolyte interface through generating protection layers or tuning the coordination environment of Zn<sup>2+</sup> ions. However, despite the much progress has been made, it still remains a daunting challenge for Zn anodes to simultaneously preserve a dense metallic deposit and fast interfacial charge transfer during cycling. Moreover, in wearable devices, one of the most promising application scenarios of Zn-ion batteries, higher demands are put forward on Zn anodes, which should be flexible as well as maintain dynamic stability at the anode/electrolyte interface. But, the Zn plating/stripping behavior on flexible substrates is rarely investigated [20].

E-mail addresses: panfeng@pkusz.edu.cn (F. Pan), wangzq@jnu.edu.cn (Z. Wang).

<sup>\*</sup> Corresponding authors.

<sup>&</sup>lt;sup>1</sup> H. Chen and Z. Guo contributed equally to this work.

In this work, we report a dendrite-free flexible Zn anode (LM-AgT) based on a Galinstan liquid metal (LM) coating layer and a silvercoated Nylon textile (AgT) conductive substrate. The LM demonstrates good affinity for the silver on the AgT and is able to tightly adhere to the anodes under deformation. Unlike routine solid/liquid anode/electrolyte interfaces, the LM interlayer establishes a liquid/liquid contact between the anode and electrolyte [21,22]. Thus, the interfacial charge transfer is significantly boosted, resulting in a very small Zn redox overpotential. More important, the LM interlayer supports a "delayed" Zn nucleation mechanism during cycling, which contributes not only fast Zn redox kinetics but also dendrite-free Zn (002) deposition. Such merits of the delayed nucleation are detailedly discussed through a series of electrochemical analyses and density functional theory (DFT) calculations. At last, both coin-type and flexible cells are fabricated and tested to confirm the advancement of the LM-AgT anode.

# 2. Results and discussion

# 2.1. Design and Characterization of the LM-AgT Anode

The conceptual design of the LM-AgT anode is schematically depicted in Fig. 1. The LM-AgT anode (Fig. S1a) was prepared by simply brushing liquid metal on a piece of AgT substrate (Fig. S1c). We chose the AgT as the flexible current collector, considering its high electrical conductivity and the good wettability of LM on silver [23,24]. To study the positive effect of the LM interlayer on the electrochemical properties, the pristine AgT was also characterized as a comparison. The Zn deposition behavior on the two anodes was first investigated by chronoamperometry (CA) and galvanostatic techniques. In the CA profiles (Fig. S2), the current density kept growing for the bare AgT but steadied within 10 seconds for the LM-AgT, indicating that the LM provided a more stable interphase for Zn deposition. As shown in Fig. 2a, under galvanostatic deposition the AgT anode demonstrates a typical two-step plating process. The tip (-133 mV) of the voltage curve represents Zn nucleation, and the subsequent plateau corresponds to the growth of deposited Zn [25]. The AgT shows a large voltage hysteresis of about 40 mV, indicating a considerable barrier for Zn deposition. In sharp contrast, after the LM interlayer was introduced, a 10 times smaller voltage hysteresis (4 mV) is observed in the LM-AgT, meaning that the Zn plating barrier has been significantly reduced. To further elucidate this, cyclic voltammetry (CV) tests were performed on Zn|AgT and Zn| LM-AgT cells, as displayed in Fig. 2b. During the cathodic scan, Zn<sup>2+</sup> reduction on LM-AgT (-30 mV) occurred prior to that on AgT (-68 mV), which is consistent with the results of galvanostatic deposition. Furthermore, the CV of the Zn|LM-AgT cell manifests more intense peak currents, suggesting that the Zn redox kinetics on the anode is saliently accelerated. The electrochemical impedance spectroscopy (EIS) results of Zn|AgT and Zn|LM-AgT cells before and after Zn deposition were also

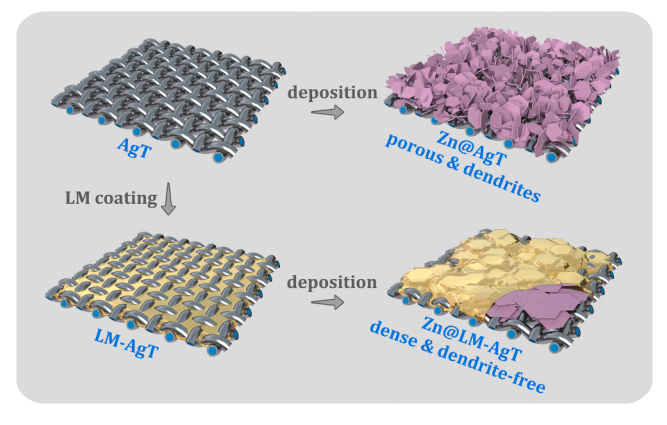


Fig. 1. Schematic illustration for the design of the LM-AgT anode.

compared. As shown in Fig. 2e, the interfacial charge transfer resistance  $(R_{ct}=R_1+R_2)$  of the Zn|LM-AgT cell  $(27.7~\Omega)$  was only one quarter of the Zn|AgT cell  $(107.5~\Omega)$  upon battery assembly, which decreased to about  $11.0~\Omega$  after  $10~mAh~cm^{-2}$  Zn deposition. We attribute the small  $R_{ct}$  and the fast Zn redox kinetics of the LM-AgT anode to the liquid/liquid contact between the LM interlayer and the bulk electrolyte. Although the two liquids are not miscible, the wettability of the LM-AgT anode in electrolyte has been effectively improved, as characterized by the contact angles of the two anodes with the electrolyte (Fig. 2c and d). It is worth noting that the wettability of LM-AgT is also much better than bare Zn anodes (Fig. S3).

The Zn (10 mAh cm<sup>-2</sup>) deposited anodes, denoted as Zn@LM-AgT and Zn@AgT were used to fabricate symmetric cells and full cells in the following study. Because the textile substrate has a 3D structure (Fig. S4) with good electrical conductivity, uniform Zn deposition is obtained on both anodes, as inferred from their smooth surfaces in Fig. S1b and S1d. However, when observed with a scanning electron microscope (SEM), the morphologies of platted Zn are quite different. For Zn@AgT (Fig. 2i), porous and loose Zn flakes were found grown on the fibers. While in stark contrast to the counterpart, dense metallic Zn formed underneath the LM interlayer of LM-AgT (Fig. 2j). The results stringently prove that the LM interlayer favors compact and dendritefree Zn deposition, which is essential for high reversibility and a long battery lifespan. Such a deposition mechanism of LM-AgT will be detailedly discussed in the following part. The average Coulombic efficiency of the two samples was assessed in accordance with the approach suggested by Xu et al. [26]. The LM-AgT exhibits a respectable average CE of 94.3% for the first 20 cycles, as shown in Fig. S5. However, an unexpected battery short-circuit causes the CE test for the bare AgT to fail. The galvanostatic Zn plating/stripping performance was investigated through the symmetric cells assembled with Zn@AgT and Zn@LM-AgT, respectively. Fig. 2h shows the long-term cycling voltage curves at 2 mA cm<sup>-2</sup>. The over potential of Zn@LM-AgT increased slightly from 43 to 97 mV over 700 h, while in the scenario of Zn@AgT, its over potential rapidly grew to about 300 mV in 200 h and became shortcircuited soon afterwards. In the meantime, under different current densities (Fig. 2g), the Zn@LM-AgT reveals not only smaller polarization, but also higher critical current compared with its counterpart. It can survive a 20 mAh cm<sup>-2</sup> deposition current without short circuit, but the Zn@AgT is dead under 3 mAh cm<sup>-2</sup>. The activation energy (Ea) is used to evaluate the charge transfer barrier on the anodes [27]. As calculated by the Arrhenius relationship between R<sub>ct</sub> (Fig. S6) and temperature, the Ea is determined to be 46.22 and 52.38 kJ mol<sup>-1</sup> for the Zn@LM-AgT and Zn@AgT, respectively (Fig. S7). A smaller Ea is obtained with the LM interlayer, indicating it facilitates the transfer and the deposition kinetics of Zn<sup>2+</sup>. The Tafel plots of the symmetric cells were further tested, as shown in Fig. 2f. Benefited from the LM interlayer, an increased corrosion potential is observed in the Zn@LM-AgT anode, suggesting a higher resistance against HER in aqueous electrolyte. Moreover, the LM droplet still demonstrates a shiny appearance after being immerged in electrolyte for 10 days (Fig. S8), confirming its stability as an anode protection layer. Collectively, the LM has shown its merits in stabilizing the anode/electrolyte interface, accelerating Zn redox, and suppressing dendrite growth.

# $2.2.\ \ Zn\ Deposition\ Mechanism\ of\ the\ LM-AgT\ Anode$

It has been reported that in aqueous electrolytes, Zn (100) and Zn (101) crystal planes on bare Zn anode grow faster [28,29], which usually leads to typical flaky dendrites like in Fig. 2i. While when the Zn (002) plane dominates, a dense structure parallel aligned to the substrate will be obtained. Therefore, to further investigate the influence of the LM interlayer on Zn deposition, X-ray diffraction (XRD) tests were performed on the anodes. Fig. 3a shows the XRD patterns of Zn@LM-AgT and Zn@AgT with different deposition capacities. For Zn@AgT, (101) is the dominated Zn crystal plane and the ratio of the integrated

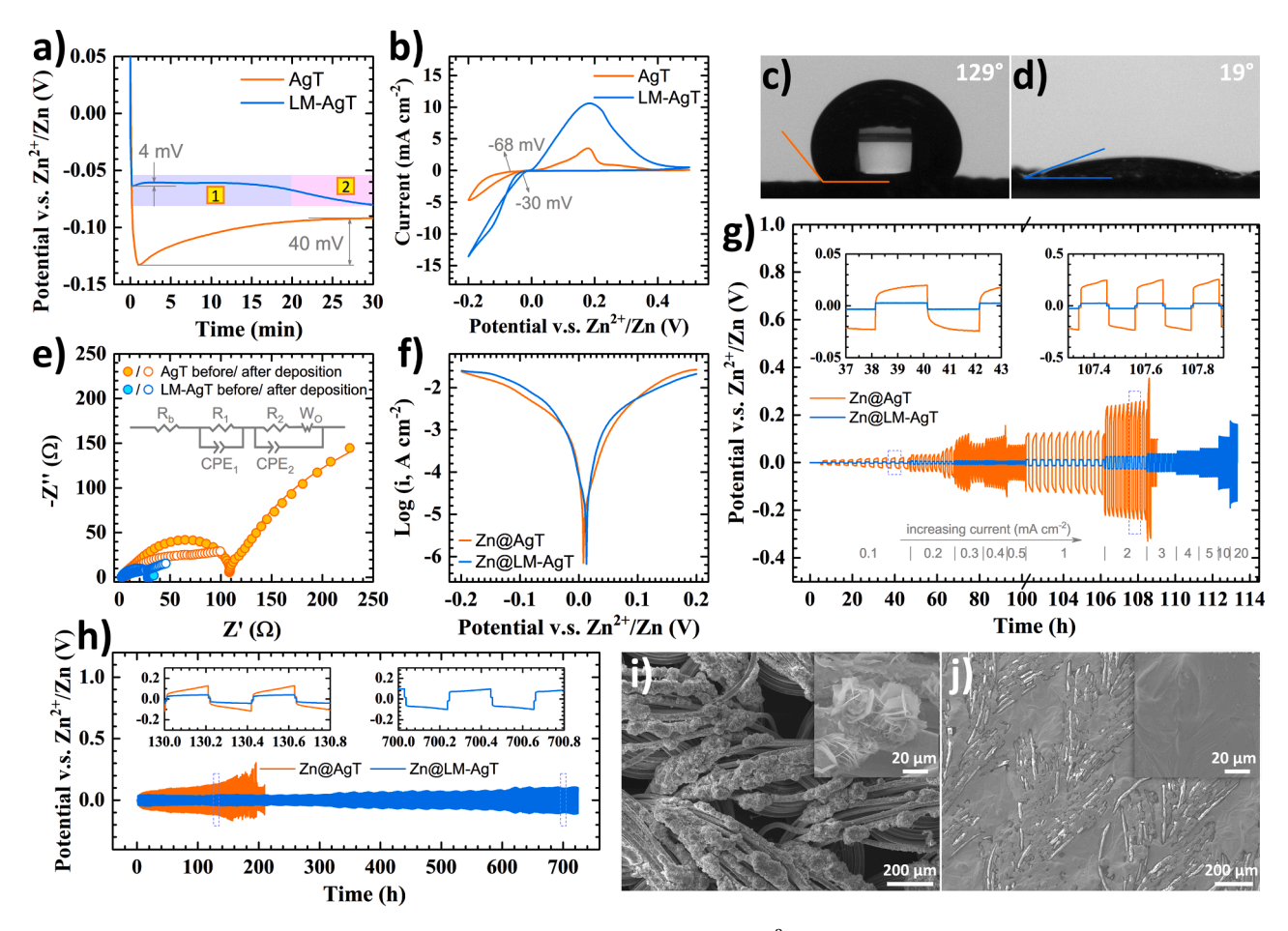


Fig. 2. a) Galvanostatic voltage profiles of Zn deposition on AgT and LM-AgT anodes at 2 mA cm $^{-2}$ . b) CV curves of Zn|AgT and Zn|LM-AgT cells at a scan rate of 0.5 mV s $^{-1}$ . Optical images of the contact angles for c) AgT and d) LM-AgT with ZnSO<sub>4</sub> electrolyte. e) EIS profiles of Zn|AgT and Zn|LM-AgT cells before and after Zn deposition at 1 mA cm $^{-2}$ , 10 mAh cm $^{-2}$ . The inset shows the corresponding equivalent circuit model. f) Tafel plots for Zn@AgT and Zn@LM-AgT symmetric cells at a scan rate of 1 mV s $^{-1}$ . g) Galvanostatic Zn plating/stripping cycles at 2 mA cm $^{-2}$ . SEM images of i) AgT and j) LM-AgT after Zn deposition.

intensities for (002) and (101) peaks ( $I_{002}/I_{101}$ ) is almost constant (about 0.45) during Zn deposition, as displayed by the histogram in Fig. 3b. For Zn@ LM-AgT, a high  $I_{002}/I_{101}$  of 4.5 is observed at the beginning of the deposition (1.0 mAh cm $^{-2}$ ), which decreases gradually to 1.6 when the deposition capacity reaches 10 mAh cm $^{-2}$ . The XRD results indicate that the above superior plating/stripping lifespan of Zn@LM-AgT anode originates from the Zn (002) deposition realized by the LM interlayer. In addition, we also found that a part of the deposited Zn alloyed with the silver coating, as the diffraction peak belonging to AgZn<sub>3</sub> (101) was detected in both samples.

To clearly inspect the Zn deposition morphology modulated by the LM interlayer, two-dimensional copper foils were further studied as the current collector instead of the 3D AgT, labeled as Cu and LM-Cu, respectively. Fig. 3c is the SEM image of the Cu current collector with 5 mAh cm<sup>-2</sup> plated Zn. A typical porous topography composed of hexagonal Zn flakes with random orientations is observed, which is agreed with the previous reports [30,31]. In order to characterize the plated Zn underneath LM, the Zn@LM-Cu was treated with ultrasonic vibration to flick off the LM layer before SEM test. As shown in Fig. 3f, large Zn flakes are compactly tiled on the Cu substrate, which indicates a planar growth and well explains the dominated Zn (002) reflection in XRD. Utilizing the substrates (such as grapheme [5]. and AgZn<sub>3</sub> [28].) with low lattice mismatch and tuning the Zn2+ flux with deliberately designed electrolytes [29]. or porous coatings [32]. are routine strategies to realize Zn (002) deposition. However, here we propose a different mechanism for the LM coated anodes. The cathodic reaction of Zn anode includes two

steps: reduction and deposition. Normally, these two steps are temporally and spatially consistent, and thus result in slow redox kinetics with random growth of Zn, as illustrated in Fig. 3d. For the anode coated with LM, which has a low Zn solubility of about 3.0 wt% at room temperature [33,34], these two steps are temporally and spatially asynchronous. As shown in Fig. 3e, the reduced Zn first dissolves in the LM interlayer (Zn<sub>I</sub>) and then crystallizes (Zn<sub>C</sub>) from it after saturation. In other words, the nucleation of crystalline Zn is delayed. Apparently, the energy barrier of Zn<sup>2+</sup> to Zn<sub>L</sub> transformation is smaller than that of Zn<sup>2+</sup> to Zn<sub>C</sub>. That is why higher redox kinetics has been observed in the LM-AgT anode with a liquid/liquid interface. More important, the delayed nucleation and growth of Zn<sub>C</sub> is restricted within the thin LM interlayer, which induces the planar growth of Zn (Fig. 3f) with exposed (002) facets. The proposed delayed nucleation mechanism is also supported by the characteristic two-step Zn deposition voltage profile of the LM-AgT in Fig. 2a. Within the initial 20 min (0.81 mg cm $^{-2}$  of reduced Zn, corresponding to 3.2 wt% in LM), it roughly retains a constant overpotential of 60 mV, representing the reduction of Zn<sup>2+</sup> to Zn<sub>L</sub>; after 20 min, the slightly increased overpotential is caused by Zn<sub>C</sub> deposition from the saturated

Furthermore, DFT calculations were also carried out to elucidate how the delayed nucleation influenced the performance of the anode. First, the interface models of the Cu and LM@Cu anodes are established (Fig. 4a-c). As demonstrated by the electron density difference maps of the LM@Cu anode (Fig. 4b and c), the unbalanced charge distribution can be clearly observed, indicating strong interactions and fast Zn

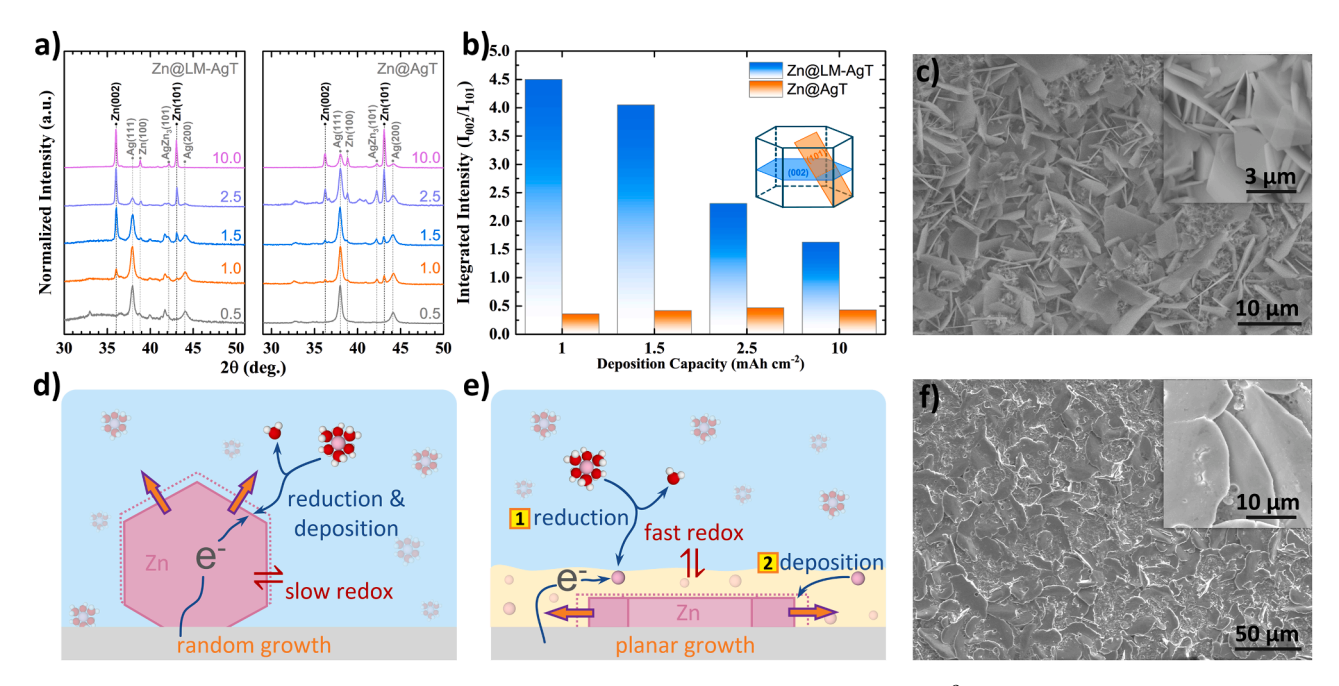


Fig. 3. a) XRD patterns of Zn@AgT and Zn@LM-AgT anodes with different Zn deposition capacities (mAh cm<sup>-2</sup>). b) The intensity ratio of Zn (002) and (101) diffraction peaks for the two anodes with different Zn deposition capacities. c) SEM images of Cu current collector after 5 mAh cm<sup>-2</sup> Zn deposition. Schematic illustrations of the Zn deposition mechanism of d) AgT and e) LM-AgT. f) SEM images of Cu current collector with LM coating after 5 mAh cm<sup>-2</sup> Zn deposition. The LM layer was flicked off by ultrasonic vibration before the SEM test.

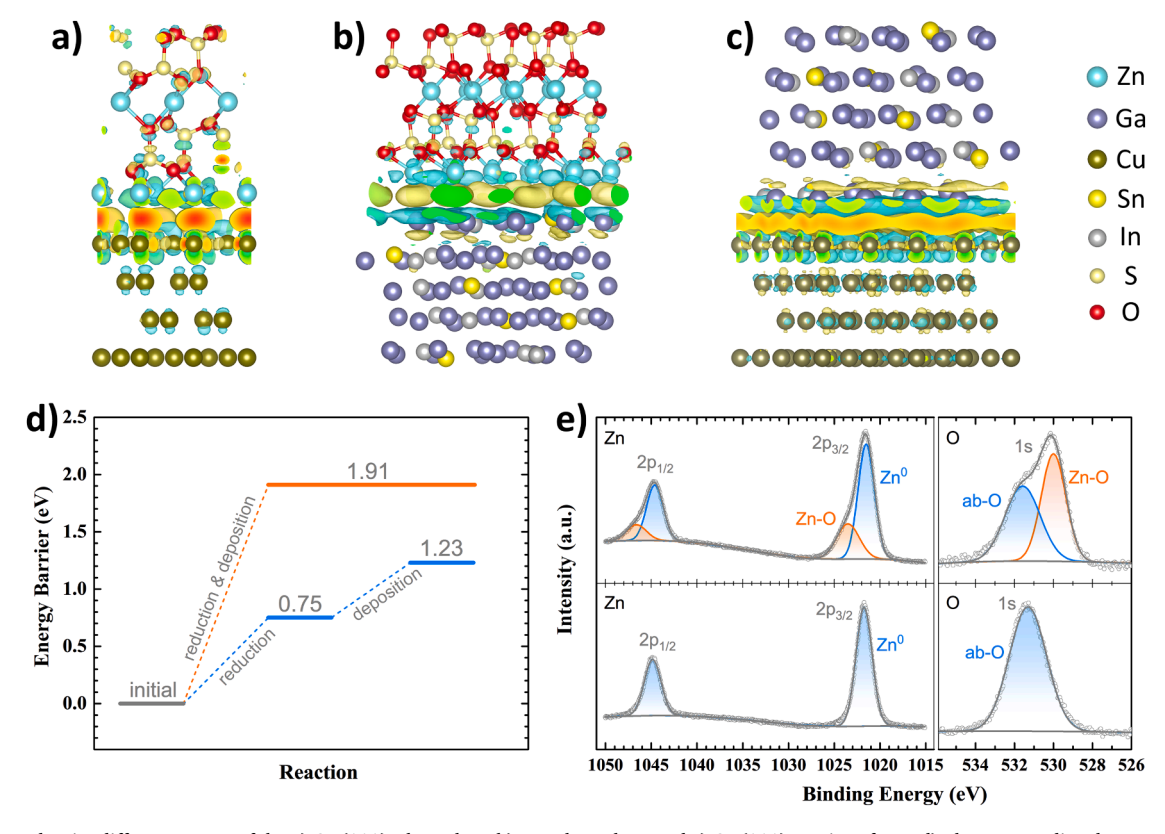


Fig. 4. Electron density difference maps of the a) Cu (111)/electrolyte, b) LM/electrolyte, and c) Cu (111)/LM interfaces. d) The DFT-predicted energy barrier of the Zn plating process with/without the LM interlayer. e) XPS analysis of Zn and O elements of the Zn@AgT (top) and Zn@LM-AgT anodes (bottom).

diffusion at the interfaces [35]. Accordingly, the energy barriers for Zn migration across the interfaces are calculated, as depicted in Fig. 4d. At the LM/electrolyte interface, the energy barrier for  $\rm Zn^{2+}$  to  $\rm Zn_L$  transformation is 0.75 eV, which increases to 1.23 eV when the  $\rm Zn_C$ 

crystalizes from the LM interlayer (Cu/LM interface). While on the bare Cu current collector, the total energy barrier for Zn reduction and deposition is 1.91 eV (Cu/electrolyte interface), which is significantly higher than the delayed nucleation process. This well explains the

higher Zn redox kinetics facilitated by the LM interlayer. Moreover, the interface energy is estimated for the Zn nucleuses with (101) and (002) facets at the Cu/LM interface, which is 17.21 and 14.37 J m<sup>-2</sup>, respectively. The relatively lower interface energy implies the priority of Zn (002) growth underneath the LM interlayer. Thus, the high Zn redox kinetics and dendrite-free Zn (002) deposition have been well expounded through the delayed nucleation mechanism from both experimental and theoretical aspects. It is also worth pointing out that the side reaction of the anode can be effectively eliminated by the LM interlayer. As shown by the X-ray photoelectron spectroscopy (XPS) results in Fig. 4e, the peaks corresponding to the oxidation state of Zn are seen in the Zn@AgT sample, but cannot be detected in the Zn@LM-AgT. The O1s peaks further confirm that no byproduct is formed during Zn deposition with the LM interlayer, as only absorbed oxygen (ab-O) is found in the Zn@LM-AgT. Because the reduced Zn is priorly dissolved in the LM interlayer, it is thus protected from passivation during plating.

# 2.3. Performance of the Full Cells

Zn-ion full batteries were assembled with an  $(NH_4)_2V_6O_{16}\cdot 1.5H_2O$  (NVO) cathode to evaluate the practicability of the LM interlayer coated anodes. The NVO cathode material was synthesized through a hydrothermal reaction of an  $NH_4VO_3$  precursor, and its phase was confirmed by XRD tests (Fig. S9). As expected, saliently improved electrochemical performance has been observed in the Zn@LM-AgT|NVO cells by virtue of the high Zn redox kinetics and dendrite-free deposition of the highly reversible anode. Fig. 5a is the CV profiles at different scan rates of the two cells with Zn@AgT and Zn@LM-AgT anodes, respectively. Owing to higher interfacial charge transfer, the Zn@LM-AgT|NVO cell demonstrates better electrochemical kinetics, as proved by its smaller voltage polarization and more intensive peak currents. Moreover, according to previous investigations [36–38], the peak current (i) is correlated to the scan rate (v):  $i = av^b$ . Once b approaches 0.5, the capacity is mainly

attributed to the diffusion-controlled process, while b close to 1 indicates that a capacitive process is dominated in the capacity contribution. By means of a logarithmic transformation (Fig. S10), the b values were calculated and marked in Fig. 5a. Because the charge storage speed of the anode has been promoted by the LM interlayer, both anodic and cathodic peaks of the Zn@LM-AgT cell reveal an elevated b value, implying an excellent high-rate capability with more capacitive contribution. The CV profiles for the first 5 cycles of the cells were also tested at 0.5 mV s<sup>-1</sup>. As shown in Fig. S11, the Zn@LM-AgT|NVO demonstrates substantially overlapped CV curves ascribed to the good reversibility of the anode, while its counterpart shows a clear peak shift due to the fast anode deterioration. Thus, better cycling stability can be envisaged for the Zn@LM-AgT|NVO cell. To confirm this, the long-term cycling performance of the cells was tested at a current density of 2.0 A g<sup>-1</sup>. As shown in Fig. 5d, benefiting from the LM interlayer on the anode, the Zn@LM-AgT|NVO cell delivers not only higher capacity, but also stabler cycling performance. The remaining capacity after 1000 cycles of the Zn@LM-AgT|NVO is 163.7 mAh g<sup>-1</sup>, which is about six times higher than the counterpart (27.1 mAh  $g^{-1}$ ). The charge/discharge curves in the selected cycles are plotted in Fig. S12 to elucidate the mechanism for capacity degradation. During cycling, the polarization of the Zn@AgT| NVO increased rapidly, indicating that the anode exhaustion should be responsible for the fast capacity fading. For Zn@LM-AgT|NVO, the voltage gap between the charge and discharge plateaus was merely raised by about 0.2 V after 800 cycles. Such good reversibility of the Zn@LM-AgT anode results in a low capacity fading rate of 0.19 % per cycle over 1000 cycles.

The inner resistance of the assembled cells was evaluated by the EIS results in Fig. 5e. Accordingly, the interfacial impedance (R<sub>1</sub>) was determined to be 860.9 and 664.4  $\Omega$  for Zn@AgT|NVO and Zn@LM-AgT|NVO, respectively, as simulated with the equivalent circuit in the inset. A smaller resistance implies better rate capability, so the performance of the two cells was further compared at different current rates.

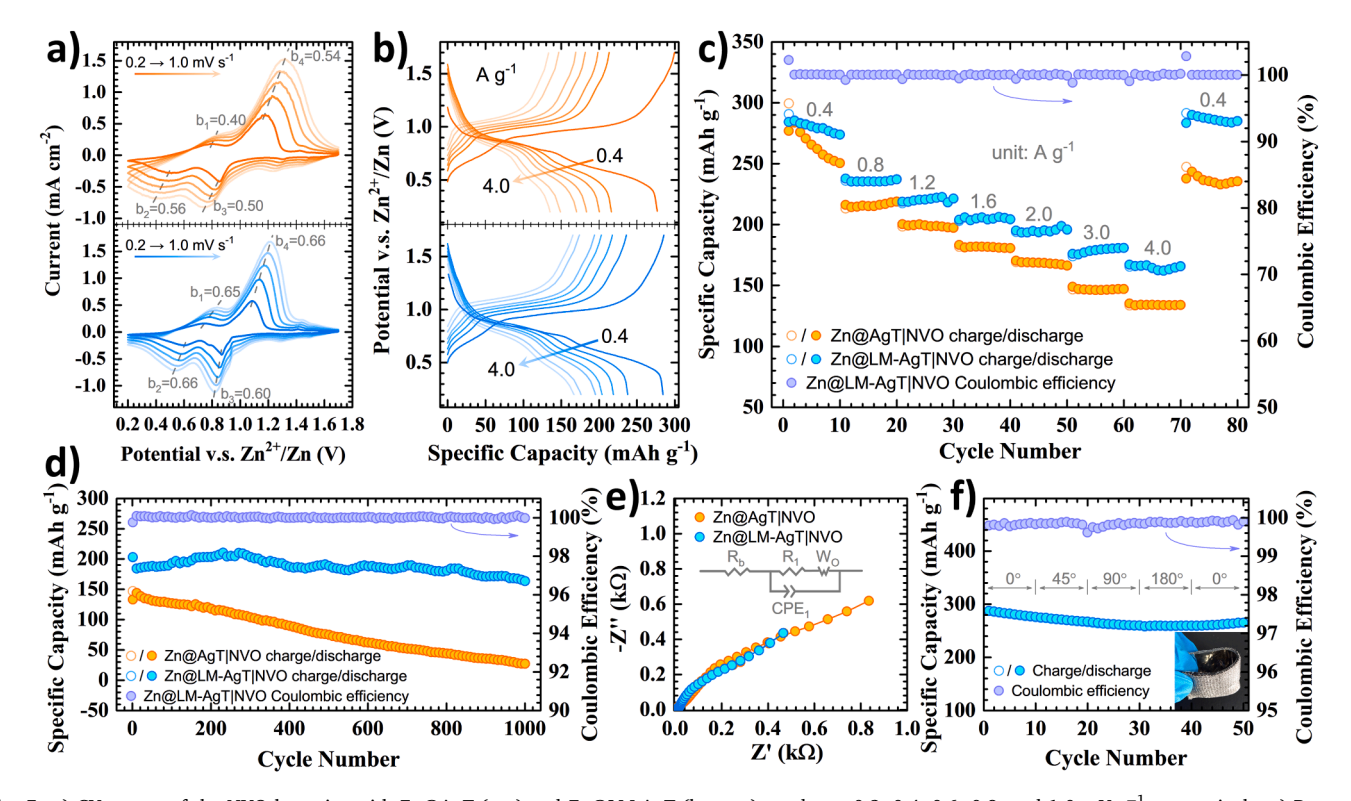


Fig. 5. a) CV curves of the NVO batteries with Zn@AgT (top) and Zn@LM-AgT (bottom) anodes at 0.2, 0.4, 0.6, 0.8, and 1.0 mV s $^{-1}$ , respectively. c) Rate performance of the NVO batteries with b) corresponding charge/discharge curves (top, Zn@AgT|NVO; bottom, Zn@LM-AgT|NVO). d) Galvanostatic cycling performance of the NVO batteries at 2 A g $^{-1}$ . e) Comparison of the EIS profiles for the NVO batteries with different anodes. f) Galvanostatic cycling performance of the flexible NVO battery at 2 A g $^{-1}$  with bending angles from 0° to 180°. Inset: an image of the assembled flexible NVO battery.

As shown in Fig. 5c, at a low charge/discharge rate of 0.4 A  $g^{-1}$ , they show a comparable capacity of about 280.0 mAh g<sup>-1</sup>. However, as the current density increases, the advantages of the LM interlayer begin to emerge. At 4.0 A g<sup>-1</sup>, the discharge capacity of Zn@LM-AgT|NVO is 165.8 mAh g<sup>-1</sup>, 24 % higher than Zn@AgT|NVO, owing to the boosted charge transfer at the LM/electrolyte interface. The charge/discharge curves at corresponding current rates are also displayed in Fig. 5b. The self-discharge of the full cells was also compared. As shown in Fig. S13, the fully charged Zn@LM-AgT|NVO and Zn@AgT|NVO release 92.2 % and 83.9 % of the capacity, respectively, after 24 h of resting. Additionally, the rested Zn@LM-AgT|NVO preserves a higher open circuit potential than the counterpart cell. As the two cells were assembled and tested in the same conditions, the above superior electrochemical performance of Zn@LM-AgT|NVO should be attributed to the unrivalled merits of the LM interlayer, such as high Zn redox kinetics and reversibility, and dendrite-free planar Zn deposition. Finally, the Zn@LM-AgT| NVO anode was implemented in a prototype flexible battery (inset of Fig. 5f) with a polyacrylamide (PAM) based gel electrolyte [39]. It keeps a stable performance with bending angles changing from 0° to 180°, exhibiting good flexibility and mechanical durability. Benefiting from the excellent deformability of the LM, the Zn@LM-AgT anode has shown its reliability in practical wearable devices.

#### 3. Conclusions

In summary, we have demonstrated a high-performance flexible anode (LM-AgT) based on a liquid metal interlayer for aqueous Zn-ion batteries. Unlike routine Zn anodes, the reduction and deposition of Zn on the LM-AgT anode are temporally and spatially asynchronous, as the reduced Zn first dissolves in the LM, and then crystalizes from it after saturation. Benefited from such a delayed nucleation mechanism, the LM interlayer simultaneously facilitates fast Zn redox kinetics and dendrite-free Zn (002) deposition, as confirmed both experimentally and theoretically. Resultantly, the Zn@LM-AgT symmetric cell manifests a stable plating/stripping cycling over 700 h with a high critical current of 20 mA cm<sup>-2</sup>, which is far beyond the counterpart anode without the LM interlayer. When coupled with the NVO cathode, the Zn@LM-AgT|NVO full cell delivers a long lifespan of over 1000 cycles with a low capacity fading rate of 0.19 ‰ per cycle. The rate capability of the Zn@LM-AgT| NVO cell is also much superior than its counterpart, especially under high current densities. Finally, due to the good deformability of the LM interlayer, flexible batteries are successfully fabricated with stable cycling performance under different bending angles. The delayed Zn nucleation mechanism provides a feasible approach to the high redox kinetics and dendrite-free deposition on arbitrary substrates.

#### 4. Experimental section

*Preparation of the flexible anodes*: A commercial silvercoated Nylon textile (Xsilver, Qingdao, China) was rinsed with ethanol and used directly as the AgT anode. The LM-AgT anode was prepared by simply brushing Galinstan alloy (68.5% Ga, 21.5% In, and 10.0% Sn by weight) on a piece of AgT substrate with a LM loading of about 25 mg cm<sup>-2</sup>. To prepare the Znloaded anodes, a LM-AgT or AgT was used as the working electrode to carry out electrochemical Zn deposition. The deposition current density and capacity were 1 mA cm<sup>-2</sup> and 10 mAh cm<sup>-2</sup>, respectively.

Synthesis of the NVO cathode material: To synthesize the  $(NH_4)_2V_6O_{16}\cdot 1.5H_2O$  cathode material, 1.5 g  $NH_4VO_3$  was dissolved in 90 mL of deionized water at  $80^{\circ}C$  by vigorous stirring, into which hydrochloric acid was added dropwise until the pH decreased to 1.5. After stirring for 30 min, the solution was transferred into a Teflon-lined stainless-steel autoclave and heated at  $180^{\circ}C$  for 24 h. When cooled down to room temperature, the precipitate was collected by filtering, and washed with deionized water to give the  $(NH_4)_2V_6O_{16}\cdot 1.5H_2O$ .

Battery assembly: Unless otherwise specified, the electrochemical

performance was investigated by CR2032 coin type cells with 2 M ZnSO<sub>4</sub> aqueous electrolyte and airlaid paper separators. The LM-AgT or AgT was cut into 16 mm round pieces for battery assembly. To prepare the NVO cathode, NVO active material was mixed with acetylene black and polyvinylidene fluoride (PVDF) in a weight ratio of 7: 2: 1, and then dispersed in N-methyl-2-pyrrolidone (NMP) to form a homogeneous slurry. The slurry was coated on a piece of Ti foil current collector and dried at 80°C in vacuum for 6 h. The active material loading in the cathode is about 1.7 mg cm<sup>-2</sup>. Coin type NVO full cells were assembled with NVO cathodes and Zn@ LM-AgT or Zn@AgT anodes. The depth of discharge of the anodes in the full cells at  $0.4 \text{ A g}^{-1}$  is estimated to be 5 %. The PAM gel electrolyte was used to fabricate the flexible batteries. Specifically, 4.6 g ZnSO<sub>4</sub>·7H<sub>2</sub>O, 2.0 g acrylamide, and 0.4 mg N, N'methylenebisacrylamide were dissolved in 6.0 mL of deionized water under continuous stirring, and then, 10 mg of ammonium persulfate was added. The mixture was injected between a NVO cathode and a Zn@ LM-AgT anode, which was heated at 50 °C for 2 h to let the electrolyte polymerize. The thickness of the gel electrolyte is 1-1.2 mm.

Characterizations: XRD patterns were collected by a Rigaku Miniflex 600 X-ray diffractometer with Cu K $\alpha$  radiation. SEM tests were performed with a Hitatchi TM3030 Tabletop Microscope. CA, CV, EIS, and Tafel plots were measured through a CHI-650E electrochemical working station. XPS results were tested with Thermo Scientific K-Alpha+equipment. The Zn plating/stripping tests and battery cycling were performed with a LANHE CT3002A cell test system.

Computation details: First-principles calculations were carried out using DFT with the generalized gradient approximation (GGA) of Perdew-Burke-Ernzerhof (PBE) implemented in the Vienna Ab-Initio Simulation Package (VASP). The valence electronic states were expanded on the basis of plane waves with the core-valence interaction represented using the projector augmented plane wave (PAW) approach and a cutoff of 520 eV. The brillouin zone integration was sampled with  $2\times2\times1$  K-point meshes for geometry optimization. The structures are fully relaxed until the maximum force on each atom becomes less than 0.02 eV Å $^{-1}$ . The surface models of Zn were cleaved from the optimized bulk structures with a vacuum thickness of 15 Å to suppress the interaction between adjacent slabs. A 4  $\times$  4 supercell with 4 atomic layers was used in our calculations.

# CRediT authorship contribution statement

**Huige Chen:** Conceptualization, Methodology, Writing – original draft. **Zechu Guo:** Data curation, Software. **Huashan Wang:** Conceptualization, Data curation. **Weiyuan Huang:** Conceptualization, Data curation. **Feng Pan:** Supervision, Writing – review & editing, Funding acquisition. **Ziqi Wang:** Supervision, Writing – review & editing, Funding acquisition.

# **Declaration of Competing Interest**

The authors declare that they have no known competing financial interests or personal relationships that could have appeared to influence the work reported in this paper.

# Data availability

Data will be made available on request.

# Acknowledgements

This work is supported by the National Natural Science Foundation of China (52102255), the Guangdong Basic and Applied Basic Research Foundation (2022A1515010745), the Guangzhou Basic and Applied Basic Research Foundation (202201010492), the Fundamental Research Funds for the Central Universities (21621034), the Open Fund of

Guangdong Provincial Key Laboratory of Functional Supramolecular Coordination Materials and Applications (2020B09), the Shenzhen Fundamental Research Program (No. GXWD20201231165807007-20200807111854001), and the Soft Science Research Project of Guangdong Province (No. 2017B030301013).

#### Supplementary materials

Supplementary material associated with this article can be found, in the online version, at doi:10.1016/j.ensm.2022.11.013.

#### References

- Q. Yang, Q. Li, Z. Liu, D. Wang, Y. Guo, X. Li, Y. Tang, H. Li, B. Dong, C. Zhi, Dendrites in Zn-based batteries, Adv. Mater. 32 (2020), 2001854, https://doi.org/ 10.1002/adma.202001854
- [2] J. Hao, X. Li, X. Zeng, D. Li, J. Mao, Z. Guo, Deeply understanding the Zn anode behaviour and corresponding improvement strategies in different aqueous Znbased batteries, Energy Environ. Sci. 13 (2020) 3917–3949, https://doi.org/ 10.1039/D0EE02162H.
- [3] Q. Zhao, S. Ding, A. Song, R. Qin, F. Pan, Tuning structure of manganese oxides to achieve high-performance aqueous Zn batteries, Chinese J. Struct. Chem. 39 (2020) 388–394, https://doi.org/10.14102/j.cnki.0254-5861.2011-2765.
- [4] H. Jia, Z. Wang, B. Tawiah, Y. Wang, C.Y. Chan, B. Fei, F. Pan, recent advances in zinc anodes for high-performance aqueous Zn-ion batteries, Nano Energy 70 (2020), 104523, https://doi.org/10.1016/j.nanoen.2020.104523.
- [5] J. Zheng, Q. Zhao, T. Tang, J. Yin, C.D. Quilty, G.D. Renderos, X. Liu, Y. Deng, L. Wang, D.C. Bock, C. Jaye, D. Zhang, E.S. Takeuchi, K.J. Takeuchi, A. C. Marschilok, L.A. Archer, Reversible epitaxial electrodeposition of metals in battery anodes, Science 366 (2019) 645–648, https://doi.org/10.1126/science.2296873
- [6] P. Zou, R. Zhang, L. Yao, J. Qin, K. Kisslinger, H. Zhuang, H.L. Xin, Ultrahigh-rate and long-life zinc-metal anodes enabled by self-accelerated cation migration, Adv. Energy Mater. 11 (2021), 2100982, https://doi.org/10.1002/aenm.202100982.
- [7] H. Zhang, S. Li, L. Xu, R. Momen, W. Deng, J. Hu, G. Zou, H. Hou, X. Ji, High-yield carbon dots interlayer for ultra-stable zinc batteries, Adv. Energy Mater. 12 (2022), 2200665, https://doi.org/10.1002/aenm.202200665.
- [8] H. Zhang, R. Guo, S. Li, C. Liu, H. Li, G. Zou, J. Hu, H. Hou, X. Ji, Graphene quantum dots enable dendrite-free zinc ion battery, Nano Energy 92 (2022), 106752, https://doi.org/10.1016/j.nanoen.2021.106752.
- [9] J. Shin, J. Lee, Y. Kim, Y. Park, M. Kim, J.W. Choi, Highly reversible, grain-directed zinc deposition in aqueous zinc ion Batteries, Adv. Energy Mater. 11 (2021), 2100676, https://doi.org/10.1002/aenm.202100676.
- [10] X. Chen, W. Li, S. Hu, N.G. Akhmedov, D. Reed, X. Li, X. Liu, Polyvinyl alcohol coating induced preferred crystallographic orientation in aqueous zinc battery anodes, Nano Energy 98 (2022), 107269, https://doi.org/10.1016/j. nanoen.2022.107269.
- [11] H. Yang, Z. Chang, Y. Qiao, H. Deng, X. Mu, P. He, H. Zhou, Constructing a supersaturated electrolyte front surface for stable rechargeable aqueous zinc batteries, Angew. Chem. Int. Ed. 59 (2020) 9377–9381, https://doi.org/10.1002/ anie 202001844
- [12] Z. Wang, J. Hu, L. Han, Z. Wang, H. Wang, Q. Zhao, J. Liu, F. Pan, A MOF-based single-ion Zn<sup>2+</sup> solid electrolyte leading to dendrite-free rechargeable Zn batteries, Nano Energy 56 (2019) 92–99, https://doi.org/10.1016/j.nanoen.2018.11.038.
- [13] D. Stock, S. Dongmo, K. Miyazaki, T. Abe, J. Janek, D. Schröder, Towards zincoxygen batteries with enhanced cycling stability: the benefit of anion-exchange ionomer for zinc sponge anodes, J. Power Sources 395 (2018) 195–204, https://doi.org/10.1016/j.jpowsour.2018.05.079.
- [14] X. Shi, G. Xu, S. Liang, C. Li, S. Guo, X. Xie, X. Ma, J. Zhou, Homogeneous deposition of zinc on three-dimensional porous copper foam as a superior zinc metal anode, Acs Sustain Chem Eng 7 (2019) 17737–17746, https://doi.org/ 10.1021/acssuschemeng.9b04085.
- [15] Y. Zeng, X. Zhang, R. Qin, X. Liu, P. Fang, D. Zheng, Y. Tong, X. Lu, Dendrite-free zinc deposition induced by multifunctional cnt frameworks for stable flexible Znion batteries, Adv. Mater. 31 (2019), 1903675, https://doi.org/10.1002/ adma.201903675.
- [16] D. Li, L. Cao, T. Deng, S. Liu, C. Wang, Solid electrolyte interphase design for aqueous Zn batteries, Angew. Chem. Int. Ed. 60 (2021) 13035–13041, https://doi. org/10.1002/anie.202103390.
- [17] L. Cao, D. Li, T. Pollard, T. Deng, B. Zhang, C. Yang, L. Chen, J. Vatamanu, E. Hu, M.J. Hourwitz, L. Ma, M. Ding, Q. Li, S. Hou, K. Gaskell, J.T. Fourkas, X. Yang, K. Xu, O. Borodin, C. Wang, Fluorinated interphase enables reversible aqueous zinc battery chemistries, Nat. Nanotech. 16 (2021) 902–910, https://doi.org/10.1038/s41565-021-00905-4.
- [18] P. Sun, L. Ma, W. Zhou, M. Qiu, Z. Wang, D. Chao, W. Mai, Simultaneous regulation on solvation shell and electrode interface for dendrite-free Zn ion batteries: achieved by a low-cost glucose additive, Angew. Chem. Int. Ed. 60 (2021) 18247–18255, https://doi.org/10.1002/anie.202105756.

- [19] X. Zeng, K. Xie, S. Liu, S. Zhang, J. Hao, J. Liu, W.K. Pang, J. Liu, P. Rao, Q. Wang, J. Mao, Z. Guo, Bio-inspired design of an in-situ multifunctional polymeric solid-electrolyte interphase for Zn metal anode cycling at 30 mA cm<sup>-2</sup> and 30 mA h cm<sup>-2</sup>, Energy Environ. Sci. 14 (2021) 5947–5957, https://doi.org/10.1039/DIFF01851F
- [20] M. Zhang, P. Yu, K. Xiong, Y. Wang, Y. Liu, Y. Liang, Construction of mixed ionic-electronic conducting scaffolds in Zn powder: a scalable route to dendrite-free and flexible Zn anodes, Adv. Mater. 34 (2022), 2200860, https://doi.org/10.1002/adma.202200860.
- [21] C. Liu, Z. Luo, W. Deng, W. Wei, L. Chen, A. Pan, J. Ma, C. Wang, L. Zhu, L. Xie, X. Cao, J. Hu, G. Zou, H. Hou, X. Ji, Liquid alloy interlayer for aqueous zinc-ion battery, ACS Energy Lett 6 (2021) 675–683, https://doi.org/10.1021/ acsenersylett.0c02569.
- [22] J. Gu, Y. Tao, H. Chen, Z. Cao, Y. Zhang, Z. Du, Y. Cui, S. Yang, Stress-release functional liquid metal-mxene layers toward dendrite-free zinc metal anodes, Adv. Energy Mater. 12 (2022), 2200115, https://doi.org/10.1002/aenm.202200115.
- [23] Y. Lin, J. Genzer, M.D. Dickey, Attributes, fabrication, and applications of gallium-based liquid metal particles, Adv. Sci. 7 (2020), 2000192, https://doi.org/10.1002/advs.202000192.
- [24] M. Mohammed, R. Sundaresan, M.D. Dickey, Self-running liquid metal drops that delaminate metal films at record velocities, ACS Applied Mater. Interfaces 7 (2015) 23163–23171, https://doi.org/10.1021/acsami.5b06978.
- [25] X. Wang, J. Meng, X. Lin, Y. Yang, S. Zhou, Y. Wang, A. Pan, Stable zinc metal anodes with textured crystal faces and functional zinc compound coatings, Adv. Funct. Mater. 31 (2021), 2106114, https://doi.org/10.1002/adfm.202106114.
- [26] L. Ma, M.A. Schroeder, T.P. Pollard, O. Borodin, M.S. Ding, R. Sun, L. Cao, J. Ho, D. R. Baker, C. Wang, K. Xu, Critical factors dictating reversibility of the zinc metal anode, Energy Environ. Mater. 3 (2020) 516–521, https://doi.org/10.1002/eem2.12077.
- [27] P. Cao, X. Zhou, A. Wei, Q. Meng, H. Ye, W. Liu, J. Tang, J. Yang, Fast-charging and ultrahigh-capacity zinc metal anode for high-performance aqueous zinc-ion batteries, Adv. Funct. Mater. 31 (2021), 2100398, https://doi.org/10.1002/ adfm.202100398.
- [28] H. Lu, Q. Jin, X. Jiang, Z. Dang, D. Zhang, Y. Jin, Vertical crystal plane matching between AgZn<sub>3</sub> (002) and Zn (002) achieving a dendrite-free zinc anode, Small 18 (2022), 2200131, https://doi.org/10.1002/smll.202200131.
- [29] Y. Hao, D. Feng, L. Hou, T. Li, Y. Jiao, P. Wu, Gel Electrolyte constructing Zn (002) deposition crystal plane toward highly Stable Zn anode, Adv. Sci. 9 (2022), 2104832, https://doi.org/10.1002/advs.202104832.
- [30] P. Chen, X. Yuan, Y. Xia, Y. Zhang, L. Fu, L. Liu, N. Yu, Q. Huang, B. Wang, X. Hu, Y. Wu, T. van Ree, An artificial polyacrylonitrile coating layer confining zinc dendrite growth for highly reversible aqueous zinc-based batteries, Adv. Sci. 8 (2021), 2100309, https://doi.org/10.1002/advs.202100309.
- [31] Z. Wang, L. Dong, W. Huang, H. Jia, Q. Zhao, Y. Wang, B. Fei, F. Pan, Simultaneously regulating uniform Zn<sup>2+</sup> flux and electron conduction by MOF/ rGO interlayers for high-performance Zn anodes, Nano-Micro Lett 13 (2021), 73, https://doi.org/10.1007/s40820-021-00594-7.
- [32] Z. Zhao, R. Wang, C. Peng, W. Chen, T. Wu, B. Hu, W. Weng, Y. Yao, J. Zeng, Z. Chen, P. Liu, Y. Liu, G. Li, J. Guo, H. Lu, Z. Guo, Horizontally arranged zinc platelet electrodeposits modulated by fluorinated covalent organic framework film for high-rate and durable aqueous zinc ion batteries, Nat. Commun. 12 (2021), 6606, https://doi.org/10.1038/s41467-021-26947-9.
- [33] Q. Yu, Q. Zhang, J. Zong, S. Liu, X. Wang, X. Wang, H. Zheng, Q. Cao, D. Zhang, J. Jiang, Identifying surface structural changes in a newly-developed Ga-based alloy with melting temperature below 10 °C, Appl. Surf. Sci. 492 (2019) 143–149, https://doi.org/10.1016/j.apsusc.2019.06.203.
- [34] A. Dobosz, T. Daeneke, A. Zavabeti, B.Y. Zhang, R. Orrell Trigg, K. Kalantar Zadeh, A. Wójcik, W. Maziarz, T. Gancarz, Investigation of the surface of Ga–Sn–Zn eutectic alloy by the characterisation of oxide nanofilms obtained by the touchprinting Method, Nanomaterials 9 (2019), 235, https://doi.org/10.3390/ nano9020235.
- [35] L. Ma, Q. Li, Y. Ying, F. Ma, S. Chen, Y. Li, H. Huang, C. Zhi, Toward practical high-areal-capacity aqueous zinc-metal batteries: quantifying hydrogen evolution and a solid-ion conductor for stable zinc anodes, Adv. Mater. 33 (2021), 2007406, https://doi.org/10.1002/adma.202007406.
- [36] J. Yu, Y. Lyu, J. Liu, M.B. Effat, S.C.T. Kwok, J. Wu, F. Ciucci, Enabling nonflammable Li-metal batteries via electrolyte functionalization and interface engineering, J. Mater. Chem. A 7 (2019) 17995–18002, https://doi.org/10.1039/ C9TA03784E.
- [37] S. Luo, L. Xie, F. Han, W. Wei, Y. Huang, H. Zhang, M. Zhu, O.G. Schmidt, L. Wang, Nanoscale parallel circuitry based on interpenetrating conductive assembly for flexible and high-power zinc ion battery, Adv. Funct. Mater. 29 (2019), 1901336, https://doi.org/10.1002/adfm.201901336.
- [38] W. Li, C. Han, Y. Wang, H. Liu, Structural modulation of manganese oxides for zincion batteries, Chinese J. Struct. Chem. 39 (2020) 31–35, https://doi.org/ 10.14102/j.cnki.0254-5861.2011-2706.
- [39] L. Ma, S. Chen, H. Li, Z. Ruan, Z. Tang, Z. Liu, Z. Wang, Y. Huang, Z. Pei, J. A. Zapien, C. Zhi, Initiating a mild aqueous electrolyte Co<sub>3</sub>O<sub>4</sub>/Zn battery with 2.2 V-high voltage and 5000-cycle lifespan by a Co(iii) rich-electrode, Energy Environ. Sci. 11 (2018) 2521–2530, https://doi.org/10.1039/C8EE01415A.